# On the Evaluation of Mechanical Properties and Ballistic Performance of Two Variants of Boron Carbide

Calvin Lo[a,*], Haoyang Li[a], Geneviève Toussaint[b], James D. Hogan[a]

[a]*Department of Mechanical Engineering, University of Alberta, Edmonton, AB T6G 2R3, Canada*
[b]*Defence Research and Development Canada, Valcartier Research Center, Québec, QC, Canada*

## Abstract

A comparative study on the microstructure, rate-dependent compressive behavior, and ballistic performance of commercially available pressureless sintered boron carbide-titanium diboride (material Z) and hot-pressed boron carbide (material S) was conducted. Under quasi-static compression at rates of 1.4 to 1.6 x $10^{-4}$ s$^{-1}$, the strength was found to be 3.07 $\pm$ 0.11 GPa for Z and 4.72 $\pm$ 0.14 GPa for S. At dynamic strain rates ranging from 185 to 1152 s$^{-1}$, the compressive strength ranged from 3.56 to 4.07 GPa for material Z and 5.24 to 5.97 GPa for material S. Depth of penetration testing was performed using 7.62 mm AP M2 projectiles. The normalized ballistic efficiency of the two materials were found to be comparable at 932 m/s, while material S was superior to material Z at an impact velocity of 1078 m/s. Based on post-mortem SEM analysis of ballistic tile fragments, the inferior mechanical properties and ballistic performance of material Z are attributed to an uneven distribution of silicon impurities and a significant level of porosity.

*Keywords:* boron carbide, fracture, digital image correlation, rate-dependent uniaxial compression, ballistic, ceramic, depth of penetration

*Corresponding author
Email address:* `clo2@ualberta.ca` (Calvin Lo)

## 1. Introduction

Boron carbide ($B_4C$) is attractive as a structural material due to its low density ($2.52\,g/cm^3$)[1], high compressive strength ($\sim 3$ to $5$ GPa)[2, 3], high hardness ($\sim 25$ to $30$ GPa)[4], and high Young's modulus ($\sim 450$ to $550$ GPa)[5]. An important application for boron carbide is in the field of protective equipment, where it is utilized as the strike face material in composite-based personnel and vehicle armour systems. However, wider application of boron carbide has largely been limited by its low fracture toughness ($K_{1c} = 2.7$ to $3.6\,MPa\sqrt{m}$[4, 6]) and the difficulties associated with sintering boron carbide to high densities[7, 8]. As a result, much research attention has been focused on incorporating additives to both aid in the densification of monolithic $B_4C$[9, 10, 11, 12], as well as to form composite $B_4C$ materials with improved properties[13, 14, 15]. In particular, boron carbide-titanium diboride ($B_4C$-$TiB_2$) composites have been found to be a promising alternative material due to their excellent mechanical properties[16, 17].

$B_4C$-$TiB_2$ composites, which have been fabricated from $B_4C$ and $TiB_2$ powders [18, 19] or through in-situ reactions with other additives[20, 21, 22], consist of a $B_4C$ matrix reinforced by titanium diboride ($TiB_2$) particles. The introduction of a secondary $TiB_2$ phase into $B_4C$ has been shown to improve sinterability[20, 22], while also enhancing a range of mechanical properties[16, 17, 18, 23]. Many studies have focused on the increased flexural strength and fracture toughness of $B_4C$-$TiB_2$ composites in comparison to monolithic $B_4C$[16, 24, 25]. This toughening effect has been attributed to a combination of crack bridging and deflection due to the reinforcing $TiB_2$ particles[20, 24, 26], as well as microcracking at the weak boundaries between $B_4C$ and $TiB_2$ particles[15, 18, 25]. Others have observed increased elastic modulus[15, 17] with increasing $TiB_2$ content. More recently, Yang et al.[23] found an overall improvement in the mechanical properties of Si/B co-doped $B_4C$ reinforced with $TiB_2$. These studies have established $B_4C$-$TiB_2$ as a viable alternative structural material to $B_4C$ based on its mechanical properties.

Beyond an understanding of their quasi-static mechanical properties, research on the dynamic response and direct ballistic testing of ceramics are also needed for the development of improved impact models and protection materials. To this end, much work has been directed at understanding the behavior of monolithic $B_4C$ under dynamic loading conditions. Using the split-Hopkinson pressure bar (SHPB) to reach strain rates of $10^2$ to $10^3$ s$^{-1}$, Paliwal and Ramesh[2] and Swab et al.[3] investigated the rate-dependence of compressive strength in $B_4C$[2, 3]. Farbaniec et al.[27] and Hogan et al.[28] explored the effects of microstructural defects on failure mechanisms in boron carbide under dynamic uniaxial compression. The SHPB has also been extended to study the fracture and fragmentation behavior of boron carbide under biaxial confinement in compression[29, 30]. In terms of ballistic testing, past studies have focused on quantifying the ballistic resistance of $B_4C$[31, 32, 33], compared the performance of $B_4C$ to other armor ceramics[34, 35], studied the fracture behavior of $B_4C$ under impact loading[36, 37, 38, 39, 40], and explored the effects of different manufacturing techniques on $B_4C$ ballistic performance[41, 42]. However, until recently, there has been relatively little research on the dynamic behavior and failure of $B_4C$-$TiB_2$. Efforts toward filling this gap have come from Gao and co-workers, who studied the rate-dependent compressive and tensile behavior[43], impact response[44], and shock response[45, 46] of $B_4C$-$TiB_2$. Using the data generated from these studies, Gao et al.[47] established Johnson-Holmquist II[48] model parameters for $B_4C$-$TiB_2$. In general, more work is needed to understand the dynamic failure and ballistic performance of $B_4C$-$TiB_2$ composites.

In the present work, we compare the rate-dependent compressive behavior and ballistic performance of a $B_4C$-$TiB_2$ composite against a monolithic $B_4C$ ceramic. Uniaxial compression testing is coupled with ultra-high-speed imaging and digital image correlation to visualize fracture behavior and obtain quantitative stress-strain information across a range of strain rates. Depth of penetration tests using 7.62 mm AP M2 projectiles are conducted with in-situ ultra-high-speed imaging to evaluate the ballistic performance of the materials. In addition,

3

we perform post-mortem analysis on the targets and microscopic characterization on the ballistic fragments to gain insights into the failure characteristics of the two variants of boron carbide. In the discussion, the microstructural characterization and dynamic compression results are then linked to understand differences in ballistic performance between the two boron carbide-based ceramics.

## 2. Experimental Method

### 2.1. Materials

Two commercially available variants of boron carbide were studied: a pressureless sintered $B_4C$-$TiB_2$ composite, nominally material Z, and a hot-pressed monolithic $B_4C$ ceramic, nominally material S. The materials were received as square tiles measuring 10 x 10 cm with a thickness of $6.42 \pm 0.02$ mm for S and $6.20 \pm 0.04$ mm for Z. In this section, we detail the equipment and procedure used for the microstructural characterization, mechanical testing, and the depth of penetration testing.

### 2.2. Scanning Electron Microscopy

Scanning electron microscopy (SEM) was used to investigate microstructural features (e.g., secondary phases) on mechanically polished surfaces of the two boron carbide variants. SEM studies were also carried out on recovered ballistic fragments of the two variants of boron carbide to identify the fracture surface characteristics and failure mechanisms. A Zeiss Sigma FESEM equipped with an energy-dispersive x-ray spectroscopy (EDS) detector was used to perform the SEM analysis in this study. The electron high tension (EHT) voltage was set at 10 kV for the Inlens detector and 20 kV for the EDS detector. The working distance was set to approximately 8.5 mm to accommodate the detecting angle of the EDS probe. The Inlens detector was used to image the microstructural features on the intact and fracture planes (field-emission), and the EDS detector was used to map out the elemental composition of the corresponding fields. The

EDS map data was analyzed using the AZtec software developed by Oxford instruments. Samples were prepared using Au/Pd coatings with a thickness of $\sim$ 8 nm to enhance conductivity. At least 15 regions across five fragments for both materials from the ballistic experiments were examined to collect representative observations.

## 2.3. X-ray Diffraction

X-ray diffraction (XRD) was used to identify the phases present in the two variants of boron carbide. This information was also used to verify the secondary phases observed under EDS mapping; contaminants picked up during the recovery process may be eliminated as constituents of the ballistic fragments. XRD spectrums were obtained using a Rigaku XRD Ultima IV system with a Cu K$\alpha$ beam source, a scan rate of $1.5°$/min, a step size of $0.015°$, and a scanning range between 5 and $80°$. The $2\theta$ range was chosen based on typical boron carbide materials, where peaks typically occurred after $10°$[49]. The apparatus was operated at 40 kV and 44 mA on a standard stage, and the $2\theta$-$\theta$ spectrum was obtained using SmartLab Studio-II software. Finally, the phases were matched using the JADE software with the K-$\alpha2$ background signal removed.

### 2.3.1. Indentation Testing

Nanoindentations at loads of 50 to 100 mN were performed on both materials using a ZHN Universal Nanomechanical Tester equipped with a Berkovich diamond indenter. Calibration was done on a reference fused silica before testing. Hardness measurements were made in the quasi-continuous stiffness measurement (QCSM) mode[50] and calculated according to the ISO 14577:2015 standard[51]. Measurements were taken after a normal displacement of $\sim$60 nm to eliminate the effect from the rounding of the indenter tip.

Vicker's hardness testing was also performed using a Wilson VH1102 microhardness tester following ASTM C1327[52]. Hardness testing was carried out on the polished surfaces of the machined compression specimens (described in

Section 2.4.1), and each indent was made with a 1 kg load applied over a period of 10 s. In total, 10 measurements were made for each material.

## 2.4. Mechanical Testing

### 2.4.1. Quasi-static Compression

Quasi-static uniaxial compression experiments were carried out using a servo-hydraulic MTS 810 load frame. A detailed description and schematic of the same setup used in this study can be found in Li et al.[53]. Cuboid specimens measuring 3.5 mm x 2.7 mm x 2.3 mm were machined for quasi-static and dynamic compression testing. Considerations for the specimen geometry are discussed in the following subsection on Dynamic Compression. The specimens were compressed along the longest dimension (3.5 mm) with displacement control at a constant rate of 0.0035 mm/s. A U750 Promon camera with a resolution of 1280 x 1024 pixels recording at 100 frames per second (FPS) was used to visualize the quasi-static compression experiments. In all experiments, the engineering stress was computed by dividing the force outputted from the load cell by the nominal cross-sectional area. DIC was applied to obtain strain information, as outlined later in Section 2.4.3, and the strain rates in the quasi-static tests were measured to range from 1.4 to 1.6 $\times 10^{-4} s^{-1}$.

### 2.4.2. Dynamic Compression

The dynamic uniaxial compression experiments were performed on a modified SHPB system. The theory of the SHPB system has been well documented by Song and Chen[54]. This study used the same set of bars as in Li et al.[53], where a detailed description and schematic of the setup has been provided. All bars in this setup are made of C-350 maraging steel and have a diameter of 12.7 mm. The incident and transmitted bars are 101.6 mm and 91.4 mm long, respectively. Impedance-matched tungsten carbide platens confined by Ti-6Al-4V titanium alloy were used to protect the SHPB bars from indentation by the hard ceramics. High pressure grease was applied at the interfaces between the protection platens and specimen surfaces to reduce friction and allow free lat-

6

eral expansion. The stress profile for each experiment was computed using the signal from the transmitted gauge and the transmitted bar properties. As in the quasi-static compression experiments, DIC was used to make surface strain measurements on the sample surface during the dynamic compression experiments. A Shimadzu HPV-X2 ultra-high-speed camera with a resolution of 400 x 250 pixels was used to image the specimen surface for the application of DIC and to visualize the failure process. The frame rate was adjusted to record from 500,000 to 2,000,000 FPS depending on the strain rate, and, therefore, the time needed to drive the specimen to failure. A REL Inc. high power LED ring light provided the lighting required to image at the 200 to 1000 ns exposure times used for these frame rates.

The same specimen geometry and dimensions were used for the dynamic compression experiments as in the quasi-static experiments. The cuboid specimen geometry has been used by other studies in the literature[27, 28, 30, 55], and past researchers have shown the viability of cuboid specimen geometries in SHPB tests [56, 57]. In addition, cuboids were chosen so that a flat surface can be imaged during mechanical testing, which enables crack speed measurements, 2D digital image correlation, and, consequently, lateral strain measurements. Since the strain rate has an inverse relationship with specimen thickness (i.e., 3.5 mm in our study), this small specimen size was chosen to achieve high strain rates while maintaining equilibrium and a constant strain rate[54]. Conventionally, the specimen should be much smaller than the bar to ensure force equilibrium [54]. In addition, due to the high strength of these materials, the cross-sectional area of the specimen must also be limited to ensure that the peak stress delivered by the SHPB is greater than the compressive strength of the materials. Based on these reasons, we have chosen our specimen dimensions.

In order to access a range of dynamic strain rates, we varied the striker length (from 152 to 304 mm), as well as the dimensions and type of pulse shaper used. Tin and high density polyethylene (HDPE) pulse shapers were employed in this study because they were found to produce near triangular pulses. The pulse shaping configurations used to achieve three distinct sets of

7

dynamic strain rates ranging from 185 to 1152 $s^{-1}$ are summarized in Table 1. The pulse shaper diameters and thicknesses in Table 1 were chosen to achieve equilibrium at our desired strain rates. As noted by Naghdabadi et al.[58], the pulse shaper should be relatively small when testing brittle materials, and similar pulse shaper dimensions have also been investigated by Frew et al.[59] in a SPHB with the same diameter (12.7 mm). Figure 1 shows representative average strain-time profiles for material S at each of the three dynamic strain rates computed using DIC; it can be seen that the pulse shaping parameters used in this study generate constant strain rates. Uniform deformation and linear stress-strain curves were observed for all tests included in this paper. Additional details of the figure are discussed in the next section when presenting DIC results.

### 2.4.3. Digital Image Correlation

Digital image correlation (DIC) analysis was applied to recordings of the quasi-static and dynamic experiments in this study to acquire axial strain information. Prior to testing, speckle patterns were applied to all of the compression specimens with a fine tipped air brush to facilitate correlation. VIC2D V6 (2018) was used to perform the DIC analysis in this study. The surface was discretized with a subset size of 31 x 31 pixels and a step size of 7 pixels. Correlation was carried out using the zero-normalized sum of squared differences (ZNSSD) criterion with the optimized 8 tap interpolation scheme. Strains were calculated using the engineering strain tensor, and strain rates were calculated by taking the slope of the linear portions of the strain-time curves. Stress-strain curves were computed by matching the average strain profile, calculated by averaging the axial strain across the entire surface, to the stress profiles generated from the quasi-static and dynamic experiments.

For a linear elastic material, the stress and surface strain profiles should nominally match up, however, poor stress equilibrium can cause localized strains to develop. As a check for stress equilibrium during dynamic experiments, we compare the stress profile against the surface strain profiles. Figure 1 shows the

8

stress profile for a dynamic compression experiment matched up in time with the surface strain profiles computed using DIC. The average strain profile is plotted along with strain profiles generated from the six different areas of interest (AOI) illustrated by the inset in Figure 1. The strong agreement between the strain profiles from the different regions on the specimen surface and the stress profile, which is indicative of the overall response of the specimen, shows that the specimen is in good loading equilibrium. While all considerations mentioned here are analogous to classical (strain gauge) approaches to check equilibrium in the absence of imaging information, it is also a part of the authors' methods to check for good equilibrium by checking for force balance across the sample (not shown for brevity here).

### 2.5. Depth of Penetration Testing

#### 2.5.1. Target Configuration

The ballistic performance of the S and Z materials were evaluated using depth of penetration (DOP) experiments, a widely employed test method[34, 60, 61]. In DOP experiments, the ceramic to be assessed is usually bonded to a ductile semi-infinite backing material, and the assembly is then impacted by a projectile with a velocity high enough to perforate the ceramic. The residual depth of penetration in the backing material is used to evaluate the performance of the ceramic.

In the past, DOP tests have typically been carried out using aluminum alloys[42, 62] or steel[34, 63] as the backing material. Some studies have opted to use polycarbonate as a backing material instead due to its lower ballistic resistance and acoustic impedance[64, 65, 60, 61]. Since polycarbonate is softer than aluminum and steel, the projectile will penetrate deeper into the material and produce a more sensitive measurement of DOP. When comparing materials that are expected to produce similar ballistic resistance, the increased resolution in DOP can be useful for discriminating between test results[64]. In comparison to metals, the impedance of polycarbonate is also much closer to that of the fibre composites commonly used to back ceramic armors in practice, as noted by

9

Carton et al.[61]. The impedance mismatch at the tile-backing interface controls the reflection of through thickness stress waves, which can lead to large tensile stresses and have a significant influence on the amount of damage sustained by the tile[66, 67, 68, 69].

For these reasons, we chose to use polycarbonate as a backing material for the ballistic tests in the present study. Specifically, TECANAT GF20 (20% fibre-glass reinforced) polycarbonate cylinders, each with a density of 1.33 g/cm$^3$, a diameter of 150 mm, and a length of 300 mm, were used to form the backing. For the DOP experiments, the ceramics were tested in the form of as-received square tiles. To form the target, the ceramic tiles were bonded to the polycarbonate backing using AC-350 B1/2 adhesive manufactured by 3M. After the adhesive was spread between the ceramic tile and the polycarbonate cylinder, a force of approximately 44.5 N was applied with a manual press to the combined assembly and maintained for several hours. This was done to ensure even coverage of the interface and to control the thickness of the adhesive layer. The targets were then left to cure load-free for 3 to 4 days before the DOP tests. Following the ballistic experiments, DOP measurements in the polycarbonate cylinders were made using 2D X-ray imaging. Due to the slight curvature of the bullet path inside polycarbonate, the DOP was measured using the length of the bullet path instead of the horizontal depth from the polycarbonate surface.

### 2.5.2. Ballistic Test Setup

All ballistic experiments in this study were performed at the Defence Research and Development Canada Valcartier Research Center. To investigate ballistic resistance against armor piercing bullets, we employed 7.62 mm AP M2 projectiles with hardened steel cores for the DOP experiments in this study. A 60.96 cm long Krieger barrel with a twist rate of 1:10 was used to fire the projectiles at a muzzle to target distance of 4.038 m. The projectiles were loaded in 0.300 Remington Ultra Mag (RUM) cartridges packed with IMR4350 rifle powder. By varying the amount of rifle powder in the cartridges, we were able to achieve two distinct bullet velocities: $932 \pm 6$ m/s and $1078 \pm 3$ m/s (bullet

velocity measurement is discussed below).

A schematic of the testing setup is shown in Figure 2. As can be seen, the
ceramic was unconfined, and the ceramic-polycarbonate assembly was placed
in the target holder to assure perpendicularity with the barrel. The impact
event was visualized in-situ using a Shimadzu HPV-X ultra-high-speed camera
recording from 1,000,000 to 5,000,000 FPS. For each experiment, a total of
256 frames with a resolution of 400 x 250 pixels were captured. Mirrors were
positioned as shown in Figure 2 so that a single HPV-X camera can image
both the front and side views of the impact. Oehler light screens, spaced 0.996
m apart, were used to detect the passage of the projectile and to trigger the
lighting system. A Photron FASTCAM SA-Z, recording with a resolution of
1024 x 521 pixels at 40,000 FPS, was positioned at the side of the target to
visualize the impact event and the ejection of fragments over a longer timescale.
Both cameras were triggered using a laser system that detected the passage of
the bullet. Bullet velocity measurements at multiple points along the path of
the projectile were also made using the light screens and an Infinition radar
sampling at 35.509 GHz, and the frames captured by the Photron FASTCAM
SA-Z immediately prior to impact. Measurements across the three methods
were found to agree, and the velocities recorded by the Infinition radar, which
were the most consistent, are reported in this study. The projectile pitch angle
was also measured using the side view images from the Photron FASTCAM
SA-Z, and was found to be less than or equal to 3 degrees for all tests.

## 3. Results

### 3.1. Material Characterization

Figure 3 shows the $\theta - 2\theta$ spectrum of material S (Figure 3 (a) and material
Z (Figure 3 (b)). The XRD analysis confirms material S as monolithic boron
carbide without any countable secondary phases present in the material, while
material Z contains significant amount of titanium diboride. In addition, trace
amounts of iron cobalt appear at $\sim 43°$, which almost superimposes with the

11

major titanium diboride peak. This could be the result of a false signal or from environmental contamination, but it is included here for completeness.

The microstructures of material S and Z are examined on mechanically polished sample surfaces, and they are shown in Figure 4 (a) and (b), respectively. In material S (Figure 4 (a)), the brighter regions correspond to the boron carbide phase, and the darker regions correspond to other phases present in the material (i.e., undissolved silicon sintering aids and carbonaceous inclusions). The compositions of other phases are confirmed in Figure 12, and these phases account for $\sim$20% of the total area in fig. 4 (a). In general, the secondary phases in material S can be divided into two groups based on size (i.e., in terms of major diameter): inclusions in one group has a major diameter between 0.5 and 7 $\mu$m and inclusions in the other group has a major diameter between 20 and 100 $\mu$m. EDS mapping was used to confirm that the smaller sized group is comprised mainly of the undissolved silicon sintering aids, which are distributed uniformly across the material. EDS mapping also showed that the larger sized group consists of carbonaceous inclusions, and they are distributed sparsely in the material. In addition, pores are scarcely observed on the surface of material S. In contrast, dramatically different microstructure is observed for material Z (Figure 4 (b)), where the secondary phases (darker regions) constitute a larger percentage ($\sim$40%) of the total area in Figure 4 (b). These phases are a combination of undissolved silicon, carbonaceous inclusions, and titanium diboride, and they are confirmed in Figure 13 using EDS maps. The mixed secondary phases create a complex microstructure of material Z, where the sizes of the secondary phases can range from less than one micron (mainly undissolved silicon sintering aids) to several hundred microns. One particular feature we want to emphasize is that big clusters of silicon are observed in material Z, where no such phenomenon is observed in material S. In addition, pores are observed in the vicinity of the secondary phases in material Z (Figure 4 (b)), where the surfaces of these phases are very rough compared to the surrounding boron carbide. These pores may arise from mechanical polishing (especially in material Z), and they are not necessarily inherent from fabrication. Hence, we have decided not

12

to report the initial porosity level based on these SEM investigations.

The nanoindentation and Vicker's hardness testing results are summarized
in Table 2. Nanoindentation was performed on both materials to identify the
hardness of the constituent phases. In the SEM micrographs shown in Figure 4,
boron carbide shows up as bright regions and secondary phases show up as dark
regions for both materials. As an example, the yellow markings in Figure 4 represent the locations of the nanoindents within the bright regions. The samples
were measured at a maximum force of 100 mN for the bright regions and 50
mN for the dark regions. The maximum force was reduced for the dark phases
to prevent the indenter from slipping outside the smaller regions and to improve accuracy. A total of 10 and 15 indents were carried out on the bright and
dark regions, respectively. For material S, the bright regions have an average
hardness of 40.3 ± 1.4 GPa, and the dark regions have an average hardness of
34.6 ± 8.9 GPa. For material Z, the bright regions have an average hardness of
40.5 ± 1.6 GPa, and the dark regions have an average hardness of 24.6 ± 7.3
GPa. The high uncertainties of the dark regions in both materials correspond
to the higher roughness and variability in distribution of the secondary phases.
Microindentation testing showed the Vicker's hardness to be nearly identical for
the two materials, at 35.4 ± 1.5 GPa for material S and 35.4 ± 2.0 GPa.

*3.2. Quasi-static and Dynamic Compression*

Representative stress-strain curves for both materials at one quasi-static and
three dynamic strain rates are shown in Figure 5. The stress and strain profiles
were synchronized based on the time of peak stress/strain. As the specimen fails,
both profiles immediately begin dropping sharply from the maximum value,
which provides a clear point for matching (see S-B4C 02 in Fig 1). In total, 4
quasi-static and 15 dynamic compression experiments were performed for each
material. Quasi-static strain rates ranged from 1.4 to 1.6 x$10^{-4}s^{-1}$ and dynamic
strain rates ranged from 185 to 1152 $s^{-1}$. The Young's modulus, computed by
taking the slope of the stress-strain curve for each specimen, was found to be
416 ± 26 GPa for material S and 385 ± 32 GPa for material Z. The Poisson's

13

ratio, computed by averaging the slope of the quasi-static axial-lateral strain curve for each specimen, was found to be 0.15 ± 0.01 for both materials.

<sup>360</sup> To investigate rate dependence in the compressive strength, the peak stress is plotted as a function of strain rate in Figure 6. Across all strain rates probed in this study, it can be seen that material Z exhibits significantly lower compressive strength than material S. At quasi-static strain rates, the compressive strength was found to be 3.07 ± 0.11 GPa for Z and 4.72 ± 0.14 GPa for S. Quasi-

<sup>365</sup> static failure strains were 0.83 ± 0.05% for Z and 1.16 ± 0.07% for S. Both materials showed a rate-dependent increase in peak compressive strength and failure strain at the dynamic strain rates. At the dynamic strain rates, material Z has a strength of 3.56 to 4.07 GPa and material S has a strength of 5.24 to 5.97 GPa. Dynamic failure strains ranged from 0.84% to 1.13% for Z and 1.11% to

<sup>370</sup> 1.53% for S. In the current study, the approximately 20% increase in strength across the studied strain rates is consistent with the recent SHPB results by DeVries et al.[70] on coarse grain boron carbide.

### 3.3. Depth of Penetration Testing

The DOP testing parameters and results are summarized in Table 3. In

<sup>375</sup> total, 5 successful experiments were performed for material S and 6 successful experiments were performed for material Z. Figure 7 shows the DOP plotted as a function of impact velocity. The averaged reference DOP, obtained by impacting the bare polycarbonate backing at each velocity, is also included for comparison. At both impact velocities, it can be seen that material Z exhibits a

<sup>380</sup> greater DOP than material S. While the DOP for both materials near velocities of ∼932 m/s are comparable, the difference in DOP is more apparent near velocities of ∼1078 m/s. This is explored next.

Figure 8 shows four frames of the impact event captured at 2,000,000 FPS using the Shimadzu HPV-X for both materials. The first frame showing contact

<sup>385</sup> between the projectile and the tile is defined as 0 μs. In the second frame, a cloud of debris consisting of projectile erosion products and ceramic fragments expands from the point of contact. Based on the high-speed videos recorded, the

14

first radial cracks begin to propagate at ~13 μs after impact for both materials. Such cracks are difficult to observe in static frames at this resolution, but they can be more easily identified by comparing successive frames. As the projectile penetrates further into the tile, the radial cracks grow in thickness and are clearly visible by 25.5 μs. Circumferential cracks, as shown later in Figure 10, are not observed to grow during the initial 30 μs. After this time, the debris cloud expands to obscure most of the tile. By ~40 μs, the rear surface of the projectile is no longer visible and has completely penetrated the tile.

Figure 9 shows side views of the impact event recorded at 40,000 FPS using the Photron FASTCAM SA-Z, with S on the left and Z on the right. Both materials were impacted at ~932 m/s. These frames are captured over a longer time scale than in Figure 8 and are included here to show the evolution of the fragment sizes. The ejecta is initially dominated by fine, dust-like fragments in the first 100 μs after impact, as shown by the second row of frames in Figure 9. Using these high-speed videos, the velocity of the fine fragments is measured to be approximately 400 to 430 m/s. At 475 μs after impact, larger fragments begin to lift near the center of the tile. The largest fragments are slower and ejected at later time frames. This is illustrated by the large fragments near the tiles at 875 μs after impact. Since the projectile completely perforates the tile at ~40 μs after impact, much of the damage to the tile (i.e. loss of volume) actually occurs after the projectile has fully penetrated the tile.

The impact craters for material S and Z at both impact velocities are shown in Figure 10. The fragmented tiles are held in place by the adhesive used to bond the ceramic tiles to the polycarbonate backing. At the center of the craters, the dark material is melted polycarbonate that has flowed out of the perforation from the backing. General characteristics of the craters for the two materials are similar: (1) The ceramic in the immediate area around the perforation has been comminuted to a fine powder; (2) Away from the perforation, the fragmented ceramic in the crater is characterized by radial and circumferential cracks that form step-like fracture surfaces; (3) Outside of the crater, radial cracks extend to the edges of the tile. Comparing the two materials, it can be seen that the

15

craters are larger in the S tiles, with an estimated average diameter of 20.8 ± 4.7 mm$^2$, than in the Z tiles, with an estimated average diameter of 27.5 ± 0.8 mm$^2$. Material S also exhibits a greater number of radial cracks and higher crack density in comparison to material Z. This is consistent with the fragmentation behavior observed during dynamic compression experiments, as material S tends to fracture into finer fragments than Z. We did not observe any significant differences in crater characteristics between the two impact velocities for either material.

### 3.4. Fragment Characterization

Post-mortem SEM analysis is carried out on the fracture surfaces of the recovered fragments from the DOP tests at 1078 m/s, and they are shown in Figure 11, Figure 12, and Figure 13. Shown in Figure 11 (a) is the fracture surface for an S tile impacted at a velocity of 1077 m/s. In Figure 11 (a), a smooth fracture plane is observed, with intragranular fracture being the dominant fracture mode. This corresponds to the cleavage and tearing of the grain layers during fracture. Figure 11 (b) shows another site on the fracture surface, where an example of cleavage fracture in material S is indicated by yellow arrows at the center of the micrograph. Microcracks propagate through the grains with micropores developed in the vicinity of the cracks, and these are indicated by red arrows in Figure 11 (b).

Shown in Figure 11 (c) is the fracture surface for a Z tile impacted at a velocity of 1074 m/s. In contrast to the fracture plane for material S shown in Figure 11 (a), material Z exhibits a much rougher fracture surface. In addition to intragranular fracture and cleavage, porous regions are observed all over the fracture plane. The micropores have lengths ranging from less than 1 μm to 8 μm. The larger pores, with lengths ranging from 12 μm to 23 μm, are likely formed by particle pull-out, which have been observed on the fracture surfaces of B$_4$C-TiB$_2$ composites before[20]. Figure 11 (d) shows another site on the fracture surface of material Z, where micropores are indicated by yellow arrows and holes left by particle pull-out are indicated by red arrows. It is also observed

16

that micropores and particle pull-outs tend to aggregate at the sites where the

<superscript>450</superscript> crack density is high. This suggests that pore growth and particle pull-out could be active actors during an impact event which contribute to a rougher fracture surface.

Next, EDS is coupled with SEM to further examine the crack growth mechanisms and determine the composition of the secondary phases that appear to

<superscript>455</superscript> affect fracture and failure behavior. Figure 12 shows an FESEM micrograph of a fracture plane from material S (Figure 12 (a)) and the corresponding elemental maps of boron (Figure 12 (b)), carbon (Figure 12 (c)), and silicon (Figure 12 (d)). In Figure 12 (a), microcracks are observed to propagate along and through the brighter regions, while the surrounding gray areas are dominated by intra-

<superscript>460</superscript> granular fracture via grain layer cleavage. In addition, small white inclusions are distributed sparsely over the field of view and usually appear at the grain boundaries, but they do not seem to contribute to the fracture process as they are not found in the vicinity of cracks. Figure 12 (b) and (c) confirms the elemental composition of the gray and brighter regions as monolithic boron carbide and

<superscript>465</superscript> carbonaceous inclusions, respectively. In Figure 12 (c), the carbon-rich regions have flake-like shapes, while the microcracks tend to grow along the elongated side of the flake. Figure 12 (c) shows that the sparsely distributed white inclusions are silicon-rich, which could be the undissolved residue of the sintering aids. Three major conclusions can be drawn from this figure: (1) microcracks

<superscript>470</superscript> initiate and grow mostly from the carbonaceous inclusions, which acts as a weak link in the material; (2) no additional secondary phases are detected in material S; (3) silicon-rich inclusions are likely the undissolved residue of the sintering aids used to densify the material[71]. They are grain boundary features and do not appear to contribute to the fracture process.

<superscript>475</superscript> In comparison, Figure 13 shows an FESEM micrograph of a fracture plane from material Z (Figure 13 (a)) and the corresponding elemental maps of boron (Figure 13 (b)), carbon (Figure 13 (c)), silicon (Figure 13 (d), and titanium (Figure 13 (e)). Figure 13 (a) shows a triple junction of microcracks, where particle pull-outs, micropores, and secondary phases (distinguished by their

17

<sub>480</sub> brighter colors) are observed in the vicinity of the junction. The boron element map (Figure 13 (b)) shows that the microcracks pass through the monolithic boron carbide phase, but with multiple discontinuous regions (i.e., absence of boron). The absence of boron constitutes a large portion of the field of view, indicating a large amount of secondary phases existed in the material, especially

<sub>485</sub> at the fracture sites. Figure 13 (c) and (d) confirm this observation, as significant amounts of carbon and silicon occupy the void spaces in Figure 13 (b). The carbonaceous inclusions in Figure 13 (c) do not appear as flake-like as in Figure 12 (c), and they are not the sole propagating sites for the microcracks. Comparing to the sparsely distributed silicon-rich inclusions in Figure 12 (d),

<sub>490</sub> the silicon-rich regions in Figure 13 (d) appear in bulk in material Z. While a silicon peak was not detected in the XRD spectrum for material Z, the silicon-rich phase is found in significant quantities in the vicinity of microcracks on the fracture surface. This suggests that the silicon-rich phase is not evenly distributed throughout the material and can be a potential facilitator of crack growth. In

<sub>495</sub> addition, Figure 13 (e) shows two regions with highly concentrated titanium. Coupling this with the boron map and the XRD spectrum in Figure 3, it is evident that these two titanium-rich regions correspond to the titanium diboride ($TiB_2$). The propagation of the microcrack through the $TiB_2$ phase likely indicates a breakage of the $TiB_2$ particle cluster during fracture. This additional

<sub>500</sub> phase, combined with the bulk silicon-rich regions and carbonaceous inclusions, creates a more complicated fracture surface and denser microcrack networks in material Z than material S.

## 4. Discussion

### 4.1. Microstructural Effects on Material Behavior

<sub>505</sub> In this study, the elastic modulus and compressive strength were found to be lower in material Z than in material S (Figure 6) while the Vicker's hardness was found to be comparable in both materials. Past studies have found the elastic modulus to increase with increasing $TiB_2$ content in well consolidated $B_4$C-

18

TiB$_2$ composites[15, 72]. However, as shown by the intact surface in Figure 4, there is a significant level of porosity in material Z, which is known to degrade the elastic modulus and compressive strength of ceramics[73, 74]. In addition, the presence of silicon impurities may also play a role in the fracture process and reduced compressive strength of material Z. While residual silicon was also found in material S, it is sparsely distributed and largely present within the grain boundaries, as shown in Figure 12. This silicon was not found in greater quantities on the fracture surface or near microcracks, so it is not expected to contribute to the fracture process under loading. In contrast, the silicon secondary phase in material Z is present in both localized and bulk amounts. Analysis of the fracture surfaces on ballistic fragments in Figure 13 showed high concentrations of silicon content in the vicinity of microcracks. This suggests that the localized distribution of a silicon-rich phase creates potential sites for crack propagation and weakens material Z. Better performance may be achieved if the silicon content can be dispersed more evenly.

### 4.2. Ballistic Performance

The ballistic performance of ceramics in DOP tests is commonly quantified using the ballistic efficiency defined by Rosenberg et al.[34] as:

$$\text{Ballistic Efficiency} = \frac{\rho_b \times (P_0 - P_r)}{\rho_c \times t} \tag{1}$$

where $t$ is the tile thickness, $\rho_c$ is the ceramic density, $P_r$ is the residual depth of penetration in the backing after the ceramic has been perforated, and $P_0$ is the reference depth of penetration in the bare backing material. In order to account for the effect of the backing material, Savio et al.[75] proposed the normalized ballistic efficiency factor (NBE), defined as:

$$\text{NBE} = \frac{100}{\rho_c \times t} \times \left(1 - \frac{P_r}{P_0}\right) \tag{2}$$

In this definition, the residual DOP is normalized by the reference DOP, which has been shown to account for differences in backing material properties[75].

19

The NBE is preferred over the ballistic efficiency defined by Rosenberg[34] as it enables a comparison between tests performed with different backing materials in the literature.

Figure 14 shows the NBE for material S and Z plotted against projectile velocity. NBE values calculated based on DOP data from other studies[31, 42, 75, 76] involving boron carbide are also included for comparison. Note that the referenced studies all used 7.62 mm AP projectiles with steel cores, and only results with ceramic tile thicknesses ranging from 5 to 7 mm were included in the figure. Both hot-pressed and reaction bonded boron carbide have been included for completeness. From Figure 14, it can be seen that NBE generally decreases with increasing impact velocity, though this decrease appears to be less sensitive at higher velocities. Taking into account the higher impact velocities in this study, the NBE of material S compares well with the hot-pressed $B_4C$ tested in other studies. For material Z, the NBE near velocities of 932 m/s is comparable to that of material S within scatter and follows the general trend of the hot-pressed $B_4C$. However, near velocities of 1078 m/s, the NBE for material Z is clearly lower than that of material S.

The inferior ballistic performance of material Z at the higher impact velocity may be related to it's mechanical properties and fracture characteristics. A high elastic modulus is thought to extend dwell time during impact[77], so the higher elastic modulus of S tiles may contribute to a longer dwell phase when compared to Z tiles and lead to superior ballistic performance. During the penetration phase, the relatively low compressive strength of material Z may reduce the resistance encountered by the projectile as compared to material S, resulting in a greater DOP in Z. Based on the impact craters shown in Figure 10, it can be seen that the damage is also more localized in the Z tiles than the S tiles, as Z tiles show smaller impact craters and fewer radial cracks than S tiles. Material S also showed finer fragments than material Z. Therefore, material S may be more efficient at dissipating the kinetic energy of the projectile through the fragmentation and ejection of a larger portion of the ceramic tile than material Z.

20

<sub>565</sub> Lastly, it is of interest to note that the density of material Z is nearly identical to that of material S. Depending on the percentage of $TiB_2$ content, the density of $B_4C$-$TiB_2$ composites typically range from 2.53 to 3.30 g/cm$^3$[15, 18, 22, 23]. In material Z, the increase in density due to $TiB_2$ content is largely offset by the introduction of porosity. This has allowed material Z to retain a comparative <sub>570</sub> density to material S at the cost of degraded mechanical properties and ballistic performance. Nonetheless, material Z has shown comparable performance to material S at 932 m/s, and more tests at lower projectile velocities may show that it is a viable alternative to hot-pressed $B_4C$ for these velocities. In developing alternative armor materials, it is important to consider whether a <sub>575</sub> decrease in ballistic performance is worth the weight and cost savings.

## 5. Conclusion

This study compared the microstructure, rate-dependent compressive behavior, and ballistic performance of a pressureless sintered $B_4C$-$TiB_2$ composite (material Z) and a hot-pressed $B_4C$ ceramic (material S). The compressive <sub>580</sub> strength of material Z was found to be lower than that of material S through the range of strain rates accessed using quasi-static and dynamic compression experiments. Depth of penetration testing conducted using 7.62 mm AP M2 projectiles showed the two materials to be comparable at an impact velocity of 932 m/s while material S was superior to material Z at a higher impact velocity <sub>585</sub> of 1078 m/s. Post-mortem SEM analysis of ballistic fragments revealed that the fracture surface of material Z is characterized by intragranular fracture, higher levels of porosity, and localized distributions of a silicon-rich secondary phase. In contrast, the fracture surface of material S is relatively smooth and dominated by intragranular fracture. The inferior compressive properties and <sub>590</sub> ballistic performance of material Z are attributed to the level of porosity and uneven distribution of silicon impurities in the microstructure. Tailoring the microstructure of material Z to achieve a comparable density to material S and the use of sintering additives can result in tradeoffs in performance and strength.

21

These tradeoffs need to be considered in the development of improved armor ceramics.

## 6. Acknowledgment

## 7. Data Availability

The raw/processed data required to reproduce these findings cannot be shared at this time as the data also forms part of an ongoing study.

22

## References

[1] T. Roy, C. Subramanian, A. Suri, Pressureless sintering of boron carbide, Ceramics international 32 (3) (2006) 227–233.

[2] B. Paliwal, K. Ramesh, Effect of crack growth dynamics on the rate-sensitive behavior of hot-pressed boron carbide, Scripta materialia 57 (6) (2007) 481–484.

[3] J. J. Swab, C. S. Meredith, D. T. Casem, W. R. Gamble, Static and dynamic compression strength of hot-pressed boron carbide using a dumbbell-shaped specimen, Journal of Materials Science 52 (17) (2017) 10073–10084.

[4] L. Vargas-Gonzalez, R. F. Speyer, J. Campbell, Flexural strength, fracture toughness, and hardness of silicon carbide and boron carbide armor ceramics, International Journal of Applied Ceramic Technology 7 (5) (2010) 643–651.

[5] V. Domnich, S. Reynaud, R. A. Haber, M. Chhowalla, Boron carbide: structure, properties, and stability under stress, Journal of the American Ceramic Society 94 (11) (2011) 3605–3628.

[6] D. Ghosh, G. Subhash, T. S. Sudarshan, R. Radhakrishnan, X.-L. Gao, Dynamic indentation response of fine-grained boron carbide, Journal of the American Ceramic Society 90 (6) (2007) 1850–1857.

[7] S. L. Dole, S. Prochazka, R. H. Doremus, Microstructural coarsening during sintering of boron carbide, Journal of the American Ceramic Society 72 (6) (1989) 958–966.

[8] H. Lee, R. F. Speyer, Pressureless sintering of boron carbide, Journal of the American Ceramic Society 86 (9) (2003) 1468–1473.

[9] R. Lange, Z. Munir, J. Holt, Sintering kinetics of pure and doped boron carbide, Tech. rep., California Univ., Livermore (USA). Lawrence Livermore Lab. (1979).

[10] K. Schwetz, W. Grellner, The influence of carbon on the microstructure and mechanical properties of sintered boron carbide, Journal of the Less Common Metals 82 (1981) 37–47.

[11] H. Suzuki, T. Hase, T. Maruyama, Effect of carbon on sintering of boron carbide, Yogyo Kyokai-Shi 87 (1008) (1979) 430–433.

[12] R. Speyer, H. Lee, Advances in pressureless densification of boron carbide, Journal of materials science 39 (19) (2004) 6017–6021.

[13] L. Sigl, Processing and mechanical properties of boron carbide sintered with tic, Journal of the European Ceramic Society 18 (11) (1998) 1521–1529.

[14] H.-W. Kim, Y.-H. Koh, H.-E. Kim, Densification and mechanical properties of b4c with al2o3 as a sintering aid, Journal of the American Ceramic Society 83 (11) (2000) 2863–2865.

[15] Y.-j. WANG, H.-x. PENG, Y. Feng, Z. Yu, Effect of tib2 content on microstructure and mechanical properties of in-situ fabricated tib2/b4c composites, Transactions of Nonferrous Metals Society of China 21 (2011) s369–s373.

[16] V. Skorokhod, M. Vlajic, V. Krstic, Mechanical properties of pressureless sintered boron carbide containing tib 2 phase, Journal of materials science letters 15 (15) (1996) 1337–1339.

[17] S. Huang, K. Vanmeensel, O. Malek, O. Van der Biest, J. Vleugels, Microstructure and mechanical properties of pulsed electric current sintered b4c–tib2 composites, Materials science and engineering: A 528 (3) (2011) 1302–1309.

[18] L. S. Sigl, H.-J. Kleebe, Microcracking in b4c-tib2 composites, Journal of the American Ceramic Society 78 (9) (1995) 2374–2380.

[19] R. M. White, E. C. Dickey, Mechanical properties and deformation mechanisms of b4c–tib2 eutectic composites, Journal of the European Ceramic Society 34 (9) (2014) 2043–2050.

24

[20] V. Skorokhod, V. Krstic, High strength-high toughness b4c-tib2 composites, Journal of materials science letters 19 (3) (2000) 237–239.

[21] S. Yamada, K. Hirao, Y. Yamauchi, S. Kanzaki, High strength b4c–tib2 composites fabricated by reaction hot-pressing, Journal of the European Ceramic Society 23 (7) (2003) 1123–1130.

[22] A. Goldstein, Y. Yeshurun, A. Goldenberg, B4c/metal boride composites derived from b4c/metal oxide mixtures, Journal of the European Ceramic Society 27 (2-3) (2007) 695–700.

[23] Q. Yang, A. M. Çelik, J. Du, J. C. LaSalvia, C. Hwang, R. A. Haber, Advancing the mechanical properties of si/b co-doped boron carbide through tib2 reinforcement, Materials Letters 266 (2020) 127480.

[24] T. Telle, R. Brook, G. Petzow, Ion beam modification, reaction sintering, precursor pyrolysis, clean-room processing and mechanical testing–challenges in the processing of ceramic hard materials, Journal of Hard Materials(UK) 2 (1) (1991) 79–114.

[25] L. Sigl, K. Schwetz, Fracture resistance of b4c–tib2 composites, Jpn J Appl Phys 10 (1994) 224–5.

[26] E. Fendler, O. Babushkin, T. Lindback, R. Telle, G. Petzow, Modification of thermal mismatch in b4c-diboride ceramics, J. Hard Mater. 4 (3) (1993) 137–48.

[27] L. Farbaniec, J. Hogan, K. Ramesh, Micromechanisms associated with the dynamic compressive failure of hot-pressed boron carbide, Scripta Materialia 106 (2015) 52–56.

[28] J. D. Hogan, L. Farbaniec, T. Sano, M. Shaeffer, K. Ramesh, The effects of defects on the uniaxial compressive strength and failure of an advanced ceramic, Acta Materialia 102 (2016) 263–272.

25

[29] J. D. Hogan, L. Farbaniec, M. Shaeffer, K. Ramesh, The effects of microstructure and confinement on the compressive fragmentation of an advanced ceramic, Journal of the American Ceramic Society 98 (3) (2015) 902–912.

[30] L. Farbaniec, J. Hogan, K. Xie, M. Shaeffer, K. Hemker, K. Ramesh, Damage evolution of hot-pressed boron carbide under confined dynamic compression, International Journal of Impact Engineering 99 (2017) 75–84.

[31] S. Savio, K. Ramanjaneyulu, V. Madhu, T. B. Bhat, An experimental study on ballistic performance of boron carbide tiles, International Journal of Impact Engineering 38 (7) (2011) 535–541.

[32] S. Savio, V. Madhu, Effect of tile thickness and projectile velocity on the ballistic performance of boron carbide against 12.7 mm ap, Procedia Engineering 173 (2017) 286–292.

[33] S. Savio, V. Madhu, Methodology to measure the protective areal density of ceramic tiles against projectile impact, Defence Science Journal 68 (1) (2018) 76.

[34] Z. Rosenberg, S. Bless, Y. Yeshurun, K. Okajima, A new definition of ballistic efficiency of brittle materials based on the use of thick backing plates, DGM Informationsgesellschaft mbH, Impact Loading and Dynamic Behavior of Materials. 1 (1988) 491–498.

[35] M. Normandia, S. Martin, D. MacKenzie, B. Rickter, A. M. Branch, A comparison of ceramic materials dynamically impacted by tungsten carbide spheres, in: Ceramic engineering and science proceedings, Vol. 26, 2005, pp. 203–212.

[36] R. N. Katz, W. A. Brantley, Fractography of high boron ceramics subjected to ballistic loading, in: Ceramics in Severe Environments, Springer, 1971, pp. 271–282.

[37] W. A. Brantley, Microstructural and fractographic studies of boron carbide subjected to ballistic impact and static flexural loading, Tech. rep., Army Materials and mechanics Research Center Watertown MA (1970).

[38] W. Gooch, M. Burkins, G. Hauver, P. Netherwood, R. Benck, Dynamic x-ray imaging of the penetration of boron carbide, Le Journal de Physique IV 10 (PR9) (2000) Pr9–583.

[39] C. E. Anderson Jr, M. S. Burkins, J. D. Walker, W. A. Gooch, Time-resolved penetration of b4c tiles by the apm2 bullet, Computer Modeling in Engineering & Sciences 8 (2) (2005) 91–104.

[40] J. LaSalvia, R. Leavy, J. Houskamp, H. Miller, D. MacKenzie, J. Campbell, Ballistic impact damage observations in a hot-pressed boron carbide, in: Ceramic Engineering and Science Proceedings, Vol. 30, 2009, p. 45.

[41] T. Sano, M. Shaeffer, L. Vargas-Gonzalez, J. Pomerantz, High strain rate performance of pressureless sintered boron carbide, in: Dynamic Behavior of Materials, Volume 1, Springer, 2014, pp. 13–19.

[42] S. Savio, A. S. Rao, P. R. S. Reddy, V. Madhu, Microstructure and ballistic performance of hot pressed & reaction bonded boron carbides against an armour piercing projectile, Advances in Applied Ceramics 118 (5) (2019) 264–273.

[43] Y. Gao, T. Tang, C. Yi, W. Zhang, D. Li, W. Xie, W. Huang, N. Ye, Study of static and dynamic behavior of tib2–b4c composite, Materials & Design 92 (2016) 814–822.

[44] Y. Gao, W. Zhang, P. Xu, X. Cai, Z. Fan, Influence of epoxy adhesive layer on impact performance of tib2-b4c composites armor backed by aluminum plate, International Journal of Impact Engineering 122 (2018) 60–72.

[45] Y. Gao, C. Yi, W. Zhang, Experimental and analytical study of failure behavior in tib2-b4c composite under shock loading, Results in Physics 13 (2019) 102143.

27

[46] Y. Gao, C. Yi, W. Zhang, Y. Deng, Effect of tib2 on dynamic response of tib2-b4c composites under shock wave loading, International Journal of Applied Ceramic Technology 16 (1) (2019) 59–68.

[47] Y. Gao, D. Li, W. Zhang, Z. Guo, C. Yi, Y. Deng, Constitutive modelling of the tib2–b4c composite by experiments, simulation and neutral network, International Journal of Impact Engineering 132 (2019) 103310.

[48] G. R. Johnson, T. J. Holmquist, An improved computational constitutive model for brittle materials, in: AIP Conference Proceedings, Vol. 309, American Institute of Physics, 1994, pp. 981–984.

[49] A. U. Khan, A. M. Etzold, X. Yang, V. Domnich, K. Y. Xie, C. Hwang, K. D. Behler, M. Chen, Q. An, J. C. LaSalvia, et al., Locating si atoms in si-doped boron carbide: A route to understand amorphization mitigation mechanism, Acta Materialia 157 (2018) 106–113.

[50] Y. Ma, S. Mayr, Nanoindentation response of substrate-attached and free-standing single-crystalline fe7pd3 ferromagnetic shape memory thin films around the martensite transition: The impact of constraints and beyond, Acta materialia 61 (18) (2013) 6756–6764.

[51] W. C. Oliver, G. M. Pharr, An improved technique for determining hardness and elastic modulus using load and displacement sensing indentation experiments, Journal of materials research 7 (6) (1992) 1564–1583.

[52] A. C-1327-15, Standard test method for vickers indentation hardness of advanced ceramics (2015).

[53] H. Li, P. Motamedi, J. Hogan, Characterization and mechanical testing on novel $(\gamma + \alpha 2)$–tial/ti3al/al2o3 cermet, Materials Science and Engineering: A 750 (2019) 152–163.

[54] W. W. Chen, B. Song, Split Hopkinson (Kolsky) bar: design, testing and applications, Springer Science & Business Media, 2010.

28

[55] B. Paliwal, K. Ramesh, J. McCauley, Direct observation of the dynamic compressive failure of a transparent polycrystalline ceramic (alon), Journal of the American Ceramic Society 89 (7) (2006) 2128–2133.

[56] O. Sen, S. Tekalur, P. Maity, On the use of non-cylindrical specimens in a split-hopkinson pressure bar, The Journal of Strain Analysis for Engineering Design 46 (8) (2011) 866–878.

[57] X. Li, T. Zhou, D. Li, Z. Wang, Experimental and numerical investigations on feasibility and validity of prismatic rock specimen in shpb, Shock and Vibration 2016 (2016).

[58] R. Naghdabadi, M. Ashrafi, J. Arghavani, Experimental and numerical investigation of pulse-shaped split hopkinson pressure bar test, Materials Science and Engineering: A 539 (2012) 285–293.

[59] D. J. Frew, M. J. Forrestal, W. Chen, Pulse shaping techniques for testing brittle materials with a split hopkinson pressure bar, Experimental mechanics 42 (1) (2002) 93–106.

[60] M. Bolduc, B. Anctil, J. Lo, R. Zhang, S. Lin, B. Simard, K. Bosnick, M. Bielawski, A. Merati, Ballistic evaluation of nanocomposite ceramic, in: Proceedings of Personal Armour Systems Symposium PASS, 2016, pp. 19–23.

[61] E. P. Carton, B. B. Johnsen, D.-B. Rahbek, H. Broos, A. Snippe, Round robin using the depth of penetration test method on an armour grade alumina, Defence Technology 15 (6) (2019) 829–836.

[62] S. Savio, P. Senthil, V. Singh, P. Ghoshal, V. Madhu, A. Gogia, An experimental study on the projectile defeat mechanism of hard steel projectile against boron carbide tiles, International Journal of Impact Engineering 86 (2015) 157–166.

[63] R. Franzen, D. Orphal, C. Anderson Jr, The influence of experimental design on depth-of-penetration (dop) test results and derived ballistic efficiencies, International journal of impact engineering 19 (8) (1997) 727–737.

[64] P. J. Hazell, C. J. Roberson, M. Moutinho, The design of mosaic armour: The influence of tile size on ballistic performance, Materials & Design 29 (8) (2008) 1497–1503.

[65] S. Bless, Using depth-of-penetration tests to design transparent armor, Experimental Mechanics 53 (1) (2013) 47–51.

[66] D. Sherman, D. Brandon, The ballistic failure mechanisms and sequence in semi-infinite. supported alumina tiles, Journal of materials research 12 (5) (1997) 1335–1343.

[67] R. Zaera, S. Sánchez-Sáez, J. Pérez-Castellanos, C. Navarro, Modelling of the adhesive layer in mixed ceramic/metal armours subjected to impact, Composites Part A: Applied Science and Manufacturing 31 (8) (2000) 823–833.

[68] A. Tasdemirci, G. Tunusoglu, M. Güden, The effect of the interlayer on the ballistic performance of ceramic/composite armors: Experimental and numerical study, International Journal of Impact Engineering 44 (2012) 1–9.

[69] R. Goel, M. D. Kulkarni, K. S. Pandya, N. Naik, Stress wave micro–macro attenuation in ceramic plates made of tiles during ballistic impact, International Journal of Mechanical Sciences 83 (2014) 30–37.

[70] M. DeVries, J. Pittari III, G. Subhash, K. Mills, C. Haines, J. Q. Zheng, Rate-dependent mechanical behavior and amorphization of ultrafine-grained boron carbide, Journal of the American Ceramic Society 99 (10) (2016) 3398–3405.

30

[71] S. S. Rehman, W. Ji, S. A. Khan, Z. Fu, F. Zhang, Microstructure and mechanical properties of b4c densified by spark plasma sintering with si as a sintering aid, Ceramics International 41 (1) (2015) 1903–1906.

[72] C. Hwang, S. DiPietro, K. Y. Xie, Q. Yang, A. M. Celik, A. U. Khan, V. Domnich, S. Walck, K. J. Hemker, R. A. Haber, Small amount tib2 addition into b4c through sputter deposition and hot pressing, Journal of the American Ceramic Society 102 (8) (2019) 4421–4426.

[73] F. Knudsen, Dependence of mechanical strength of brittle polycrystalline specimens on porosity and grain size, Journal of the American Ceramic Society 42 (8) (1959) 376–387.

[74] K. K. Phani, S. Niyogi, Young's modulus of porous brittle solids, Journal of materials science 22 (1) (1987) 257–263.

[75] S. Savio, V. Madhu, Ballistic performance evaluation of ceramic tiles with respect to projectile velocity against hard steel projectile using dop test, International Journal of Impact Engineering 113 (2018) 161–167.

[76] P. Hazell, S. Donoghue, C. Roberson, P. Gotts, The penetration of armour piercing projectiles through reaction bonded ceramics, in: Advances in Ceramic Armor: A Collection of Papers Presented at the 29th International Conference on Advanced Ceramics and Composites, January 23-28, 2005, Cocoa Beach, Florida, Ceramic Engineering and Science Proceedings, Vol. 26, Wiley Online Library, 2005, pp. 143–150.

[77] A. Krell, E. Strassburger, Order of influences on the ballistic resistance of armor ceramics and single crystals, Materials Science and Engineering: A 597 (2014) 422–430.

31

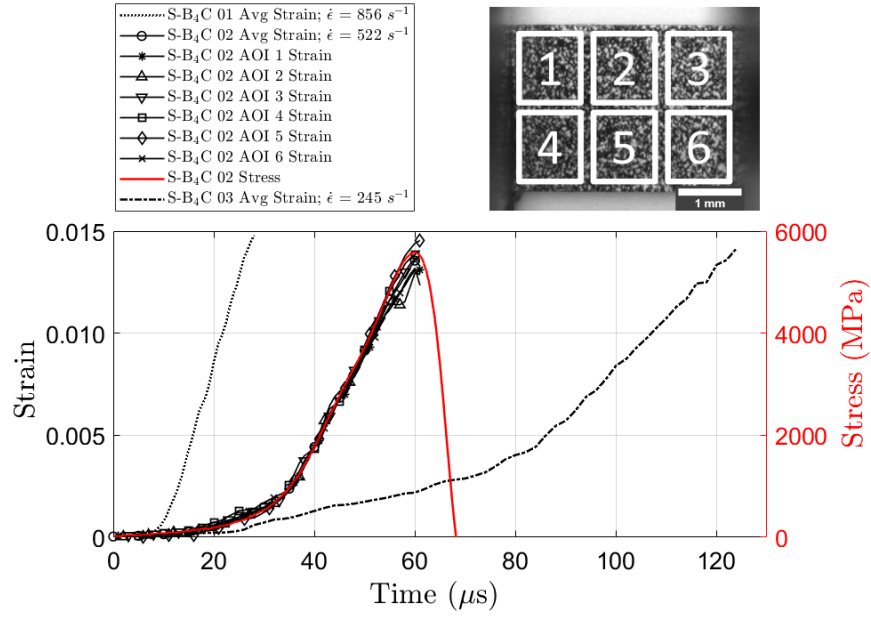## List of Figures

32

33

# 8. Figures



Figure 1: Average axial strain profiles from uniaxial compression experiments on material S at three dynamic strain rates. For specimen S-B$_4$C 02, the stress profile computed using the transmitted gauge and the local strain profiles computed from different areas of interest (AOI) are matched in time and plotted along with the average strain. The different AOI's that the local strain profiles are computed from are shown in the inset. The average strain was calculated by averaging across the entire surface.
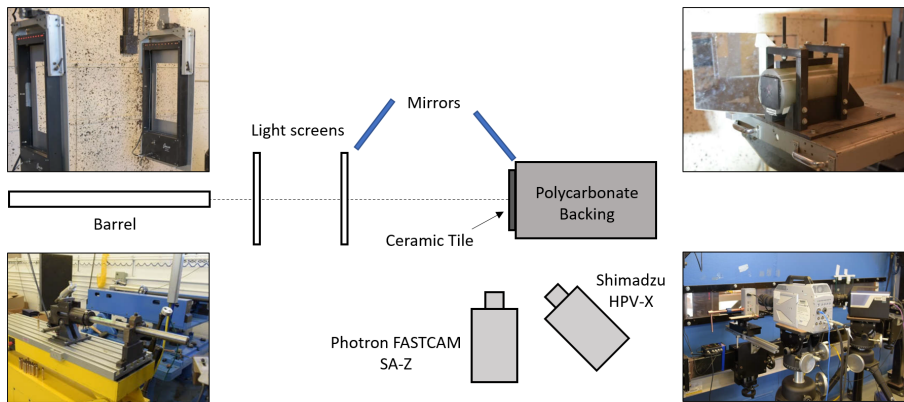
Figure 2: Schematic of the ballistic testing setup. The ceramic tile to be tested is mounted to a polycarbonate backing, which is used for DOP measurements. Light screens are used to trigger the cameras during the impact event. Two mirrors are used to allow the Shimadzu HPV-X to image the front and side views of the impact. Longer timescale events are captured from the a side view using the Photron FASTCAM SA-Z. This diagram is not to scale.
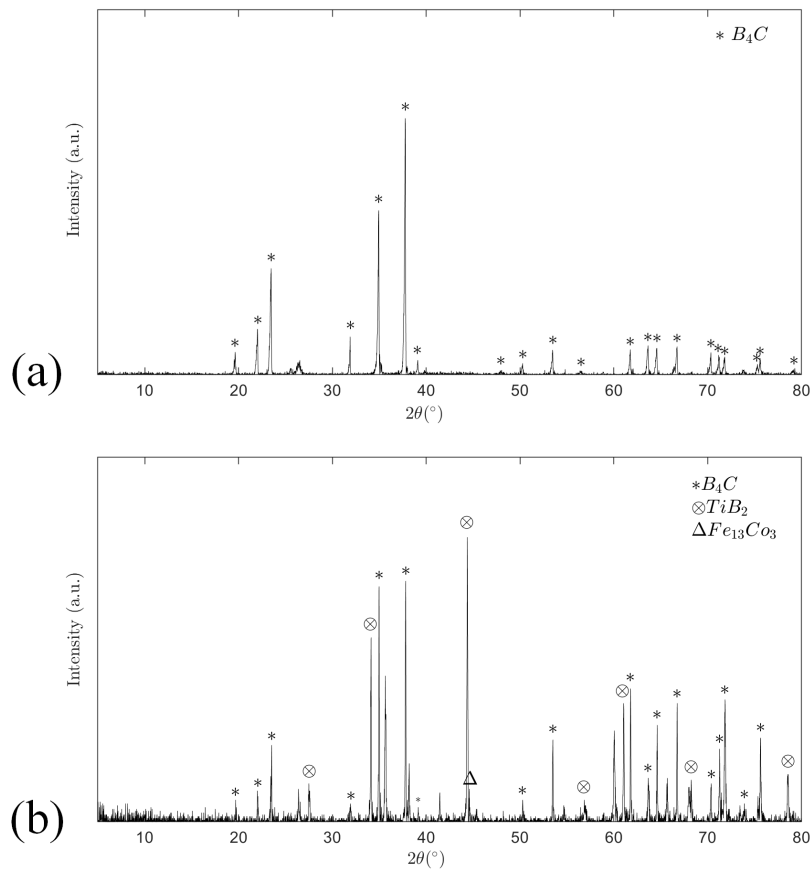
Figure 3: $\theta - 2\theta$ X-ray diffraction spectrum of (a) Material S and (b) Material Z showing the phase composition of the materials. Note that Material Z contains a significant amount of $TiB_2$ phase, while a trace amount of $Fe_{13}Co_3$ is also identified.
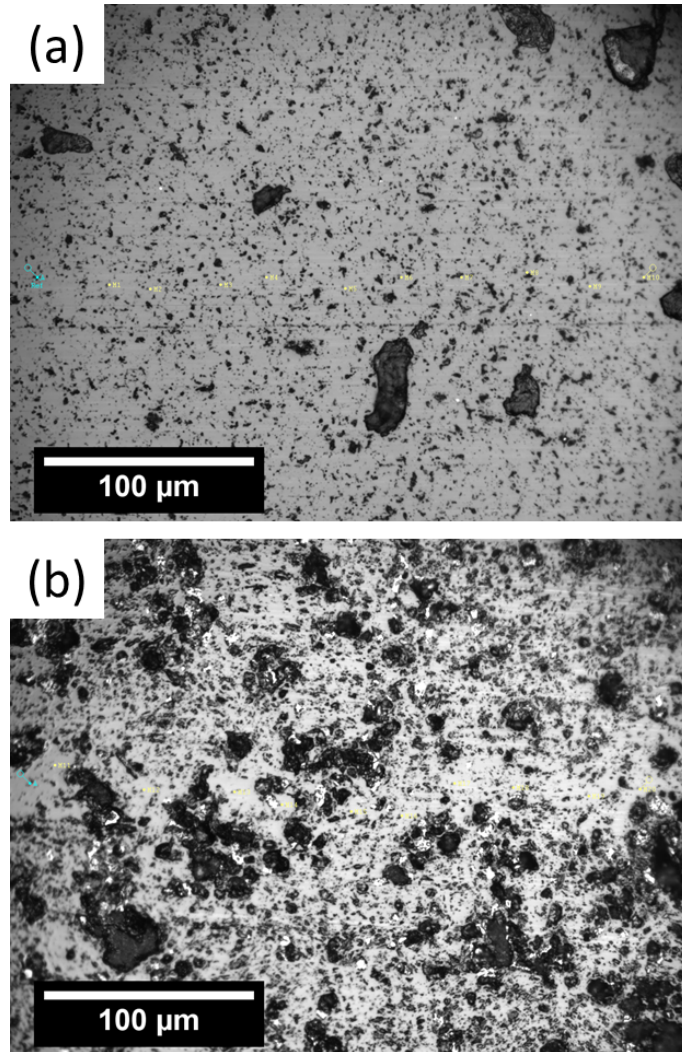
Figure 4: SEM micrograph of the mechanically polished surfaces for (a) material S and (b) material Z. The bright regions correspond to boron carbide and the dark regions correspond to various secondary phases in both materials. Yellow markings indicate the nanoindentation locations.
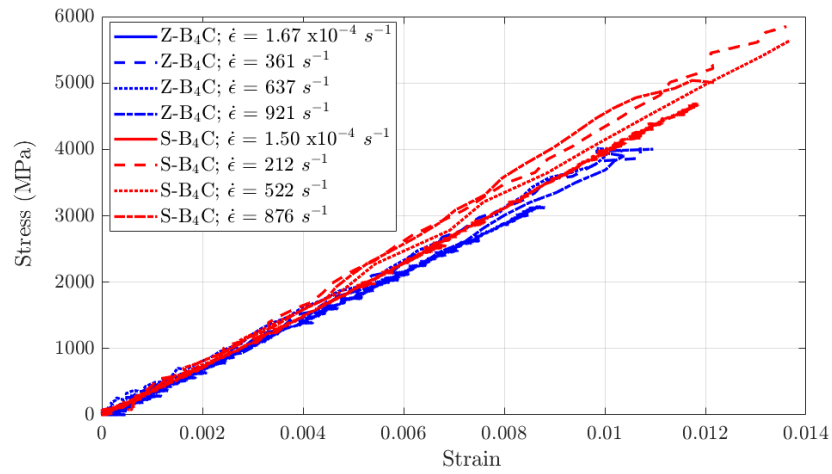
Figure 5: Representative stress strain curves for material S (red) and Z (blue) at a quasi-static strain rate and three dynamic strain rates.
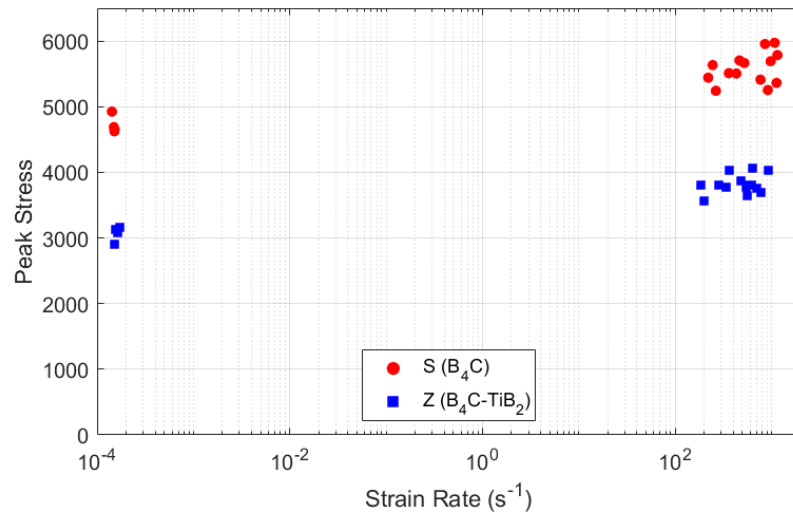


Figure 6: Peak stress plotted as a function of strain rate for material S (red) and Z (blue). The strain rate axis is in logarithmic scale.
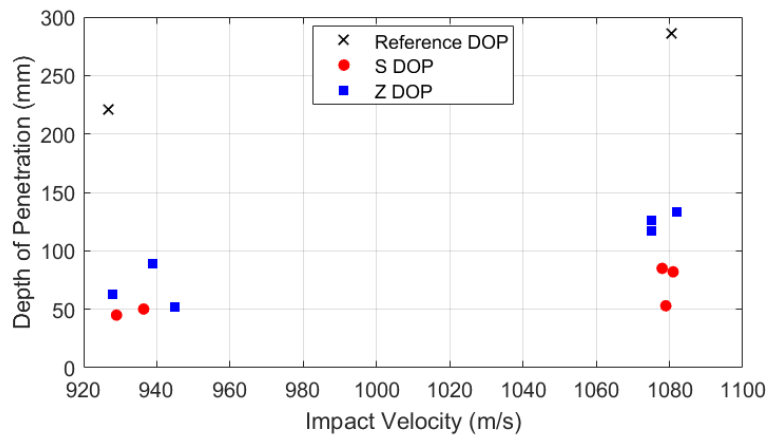
39

Figure 7: Depth of penetration (DOP) results for material S (red) and Z (blue) as a function of projectile velocity. The reference DOP obtained by impacting the bare polycarbonate backing is also included for comparison.

Figure 8: High-speed frames of the impact event captured at 2,000,000 FPS using the Shimadzu HPV-X are shown for S (left) and Z (right). Both targets were impacted at ~1078 m/s. Within each frame, the front view is shown on the left and the side view, captured using the reflection from a mirror, is shown on the right. The first frame is the first frame in which the projectile contacts the tile, and this is defined as 0 µs. The time stamps of the subsequent frames reflect the time that has elapsed since contact.
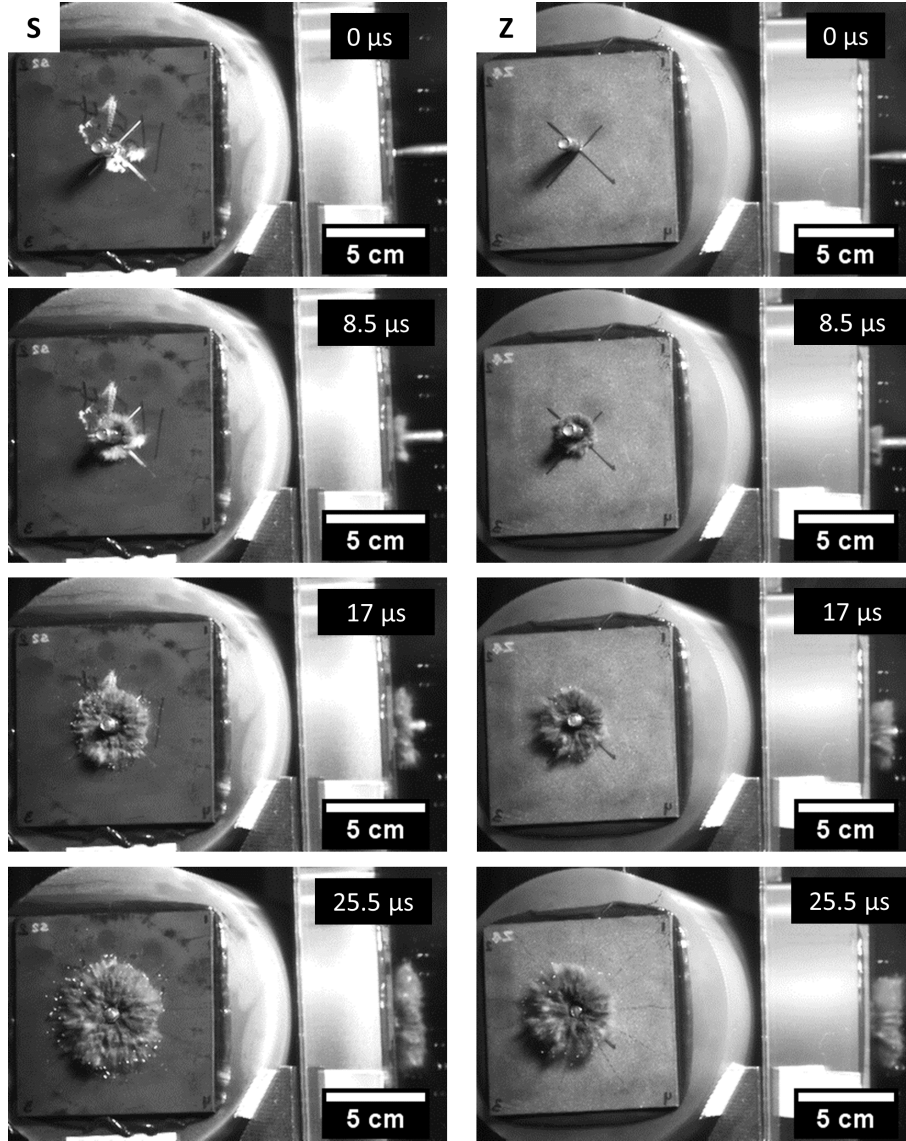
Figure 9: High-speed frames of the impact event captured at 40,000 FPS using a Photron FASTCAM SA-Z are shown for S (left) and Z (right). Both targets were impacted at ∼932 m/s. The first frame is the first frame in which the projectile contacts the tile, and this is defined as 0 µs. The time stamps of the subsequent frames reflect the time that has elapsed since contact. These frames capture the evolution of fragment sizes after the impact event.
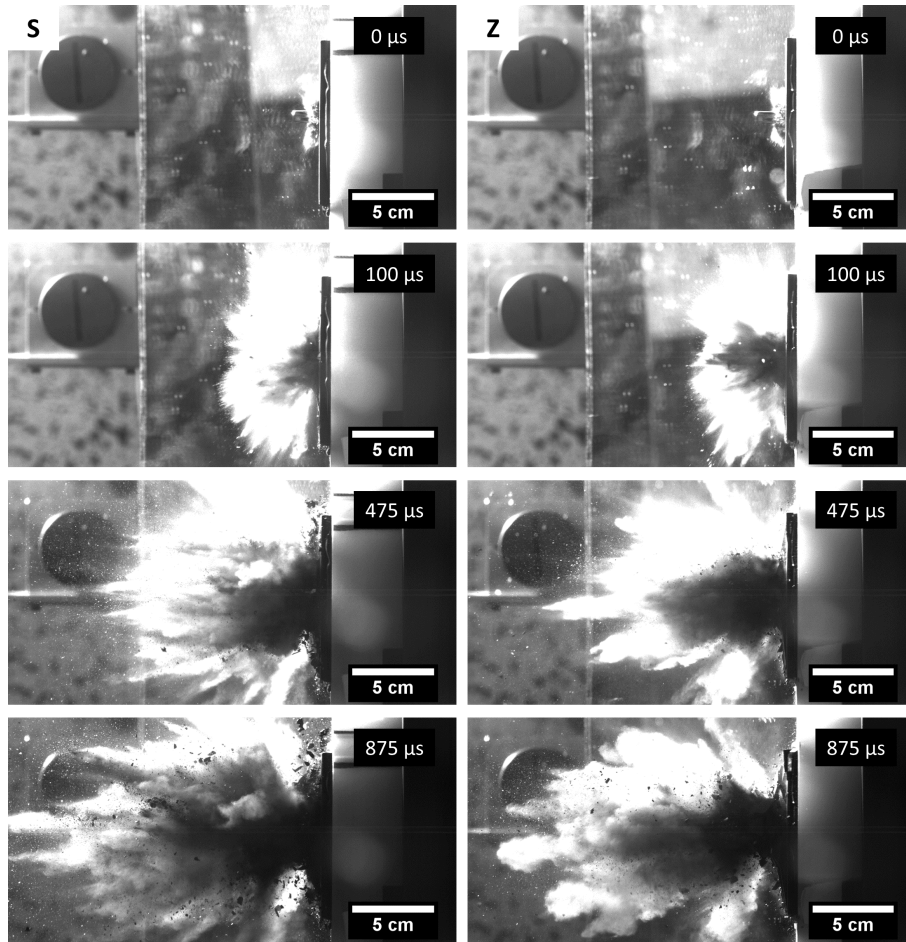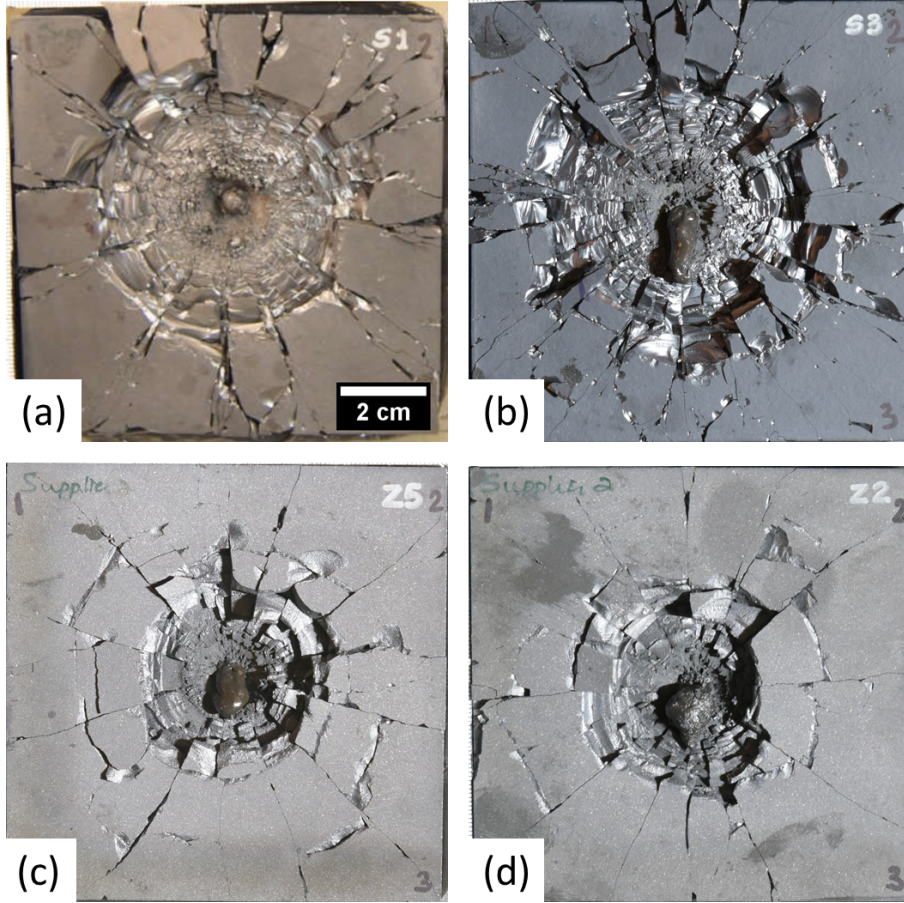
Figure 10: Post-impact view of perforated S tiles impacted at (a) 929 m/s and (b) 1079 m/s, and Z tiles impacted at (c) 928 m/s and (d) 1075 m/s. The dark material at the centre of the craters is melted polycarbonate that flowed out of the perforation after the DOP experiments.
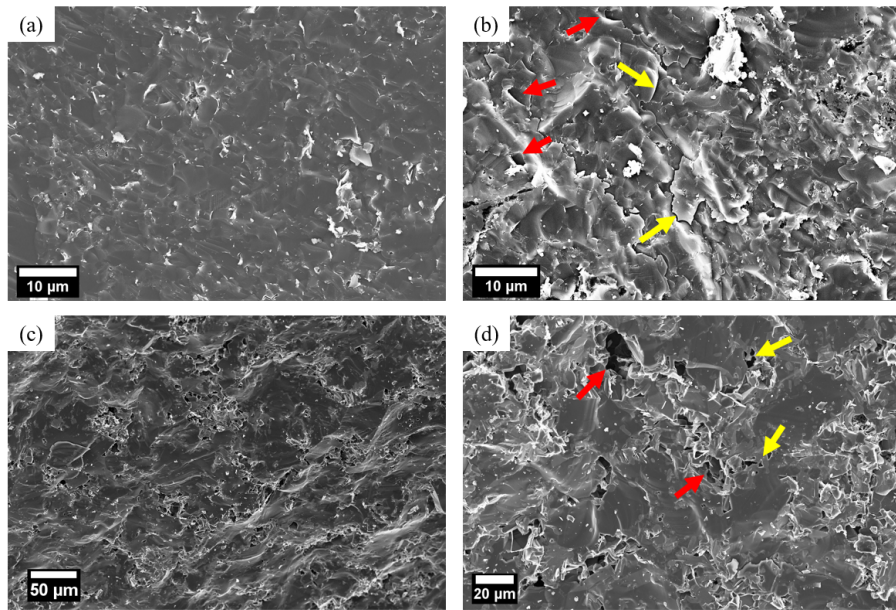
Figure 11: (a - b) Fractography of the monolithic $B_4C$ (material S) showing smooth fracture planes. Intragranular fracture corresponding to grain layer tearing is identified by yellow arrows and micrpores are indicated by red arrows. (c - d) Fractography of the $B_4C$-$TiB_2$ composite (material Z) showing rough fracture planes. A mixed mode of fracture, including intragranular, intergranular, and particle pull-out are observed. Micropores are indicated by yellow arrows and particle pull-out is indicated by red arrows.
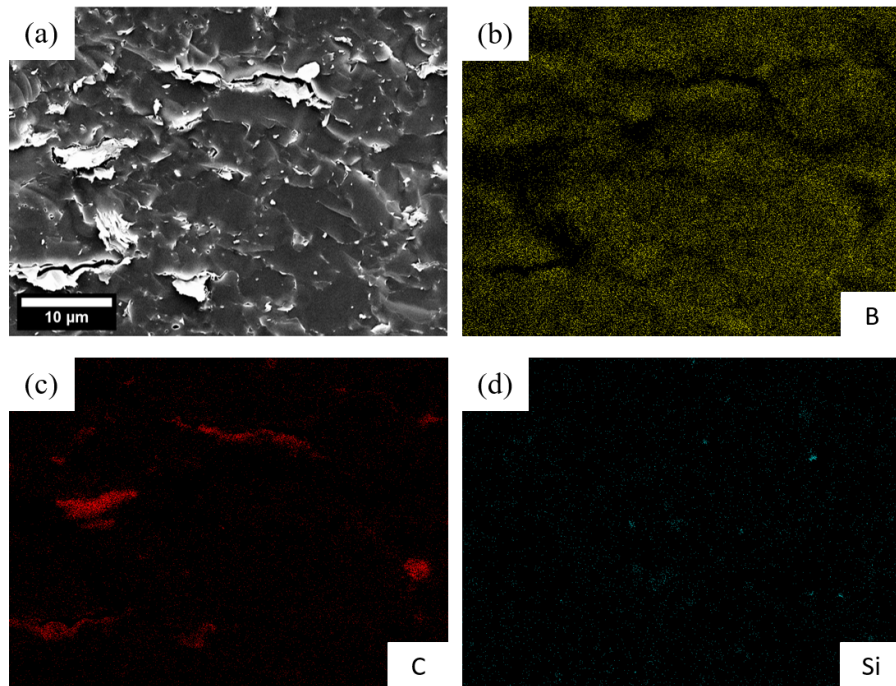
Figure 12: FESEM coupled with EDS investigation on a magnified view of material S. The fracture plane surrounding these inclusion-induced cracks remains smooth and dominated by intragranular fracture. (a) FESEM micrograph showing crack growth along the carbonaceous inclusions. EDS maps for (b) boron, (c) carbon, (d) silicon, and (e) titanium are shown.

Figure 13: FESEM coupled with EDS investigation on a magnified view of material Z. A mixed mode of fracture mechanisms is observed. (a) FESEM micrograph showing a triple junction formed by crack interaction. Pull-outs from the secondary phases and micropores are located in the vicinity of the cracks. (b) EDS map of the boron element. (c) EDS map of the carbon element. (d) EDS map of the silicon element.



Figure 14: Normalize ballistic efficiency (NBE) for material S and Z compared against NBE of boron carbide tested at different velocities from other studies[31, 42, 75, 76].

## 9. Tables

**Table 1: Pulse shaping configurations used in dynamic experiments**

| Strain Rate ($s^{-1}$) | Pulse Shaper | | | Striker Length (mm) |
| | Material | Diameter (mm) | Thickness (mm) | |
|---|---|---|---|---|
| 620 to 1100 | HDPE | 3.18 | 2.38 | 152 |
| 260 to 560 | HDPE | 3.18 | 1.59 | 304 |
| 185 to 245 | Tin | 3.97 | 1.00 | 304 |

**Table 2: Nanoindentation and Vicker's hardness results**

| Material | Nanoindentation Hardness (GPa) | | Vicker's Hardness (GPa) |
| | Bright | Dark | |
|---|---|---|---|
| S ($B_4C$) | $40.3 \pm 1.4$ | $34.6 \pm 8.9$ | $35.4 \pm 1.5$ |
| Z ($B_4C\text{-}TiB_2$) | $40.5 \pm 1.6$ | $24.6 \pm 7.3$ | $35.4 \pm 2.0$ |

**Table 3: Depth of penetration measurements for material S and Z**

| Material | Density | Tile Thickness | Projectile Velocity | Residual Penetration | Reference Penetration |
| | ($g/cm^3$) | (mm) | (m/s) | (mm) | (mm) |
|---|---|---|---|---|---|
| S ($B_4C$) | 2.49 | 6.45 | 929 | 45 | 220.7 |
| S ($B_4C$) | 2.50 | 6.38 | 936 | 50.2 | 220.7 |
| S ($B_4C$) | 2.50 | 6.40 | 1079 | 53 | 286.2 |
| S ($B_4C$) | 2.49 | 6.40 | 1078 | 85 | 286.2 |
| S ($B_4C$) | 2.49 | 6.43 | 1081 | 82 | 286.2 |
| Z ($B_4C\text{-}TiB_2$) | 2.54 | 6.17 | 928 | 63 | 220.7 |
| Z ($B_4C\text{-}TiB_2$) | 2.52 | 6.22 | 939 | 89 | 220.7 |
| Z ($B_4C\text{-}TiB_2$) | 2.55 | 6.10 | 945 | 51.8 | 220.7 |
| Z ($B_4C\text{-}TiB_2$) | 2.53 | 6.15 | 1075 | 126 | 286.2 |
| Z ($B_4C\text{-}TiB_2$) | 2.52 | 6.15 | 1075 | 117 | 286.2 |
| Z ($B_4C\text{-}TiB_2$) | 2.55 | 6.12 | 1082 | 133 | 286.2 |